Applied Physics Letters

AIP Publishing

RESEARCH ARTICLE | DECEMBER 23 2024

Narrow-bandgap titanium sesquioxide with resonant metasurfaces for enhanced infrared absorption

Special Collection: Mid and Long Wavelength Infrared Photonics, Materials, and Devices

Viktoriia E. Babicheva ; Evgeniya Lock ; Heungsoo Kim

Appl. Phys. Lett. 125, 261101 (2024)
https://doi.org/10.1063/5.0240125

Articles You May Be Interested In

Semiconductor-metal transition of titanium sesquioxide nanopowder

J. Appl. Phys. (June 2012)

Comparison of Ti 2*p* Core-Level Peaks from TiO_2, Ti_2O_3, and Ti Metal, by XPS

Surf. Sci. Spectra (July 1998)

Domain epitaxy in $TiO_2/\alpha\text{-}Al_2O_3$ thin film heterostructures with Ti_2O_3 transient layer

Appl. Phys. Lett. (June 2012)

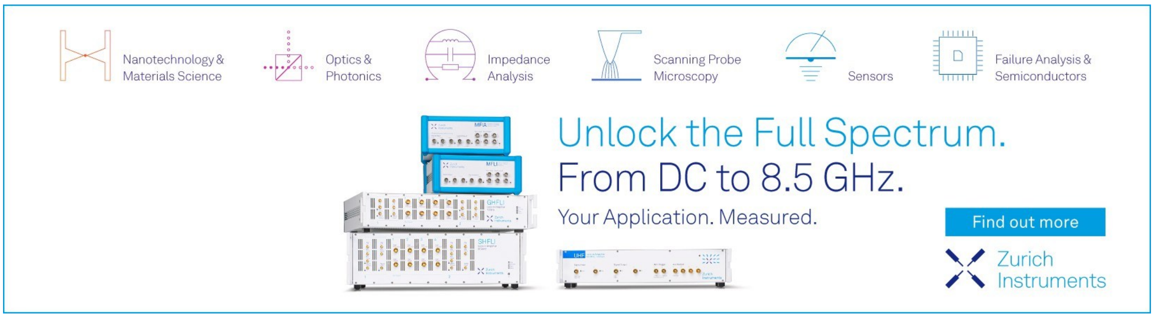

Narrow-bandgap titanium sesquioxide with resonant metasurfaces for enhanced infrared absorption

Cite as: Appl. Phys. Lett. 125, 261101 (2024); doi: 10.1063/5.0240125
Submitted: 24 September 2024 · Accepted: 12 December 2024 ·
Published Online: 23 December 2024

Viktoriia E. Babicheva,[1] Evgeniya Lock,[2] and Heungsoo Kim[2,a)]

AFFILIATIONS

[1] University of New Mexico, MSC01 1100, 1 University of New Mexico, Albuquerque, New Mexico 87131, USA
[2] Naval Research Laboratory, 4555 Overlook Ave, Washington, DC 20375, USA

Note: This paper is part of the APL Special Collection on Mid and Long Wavelength Infrared Photonics, Materials, and Devices.

[a)] Author to whom correspondence should be addressed: heungsoo.kim.civ@us.navy.mil

ABSTRACT

We report on the structural, chemical, and optical properties of titanium sesquioxide Ti_2O_3 thin films on single-crystal sapphire substrates by pulsed laser deposition. The thin film of Ti_2O_3 on sapphire exhibits light absorption of around 25%–45% in the wavelength range of 2–10 μm. Here, we design an infrared photodetector structure based on Ti_2O_3, enhanced by a resonant metasurface, to improve its light absorption in mid-wave and long-wave infrared windows. We show that light absorption in the mid-wave infrared window (wavelength 3–5 μm) in the active Ti_2O_3 layer can be significantly enhanced from 30%–40% to more than 80% utilizing a thin resonant metasurface made of low-loss silicon, facilitating efficient scattering in the active layer. Furthermore, we compare the absorptance of the Ti_2O_3 layer with that of conventional semiconductors, such as InSb, InAs, and HgCdTe, operating in the infrared range with a wavelength of 2–10 μm and demonstrate that the absorption in the Ti_2O_3 film is significantly higher than in these conventional semiconductors due to the narrow-bandgap characteristics of Ti_2O_3. The proposed designs can be used to tailor the wavelengths of photodetection across the near- and mid-infrared ranges.

Published by AIP Publishing. https://doi.org/10.1063/5.0240125

Infrared photodetectors are critical components of various advanced technologies designed to detect and respond to infrared light.[1–6] Infrared photodetectors are devices designed to detect and convert infrared radiation into measurable electrical signals by utilizing materials and structures sensitive to wavelengths in the infrared spectrum. Conventional semiconductors used in infrared photodetectors include indium antimonide (InSb), indium arsenide (InAs), and mercury cadmium telluride (HgCdTe or MCT).[7–9] These materials are chosen for their suitable bandgaps, allowing them to absorb infrared photons efficiently in Earth's atmospheric windows, including two wavelength regions: mid-wave infrared windows (MWIR: 3–5 μm) and long-wave infrared windows (LWIR: 8–12 μm). The detection mechanism typically involves excitation of electrons from the valence band to the conduction band upon absorbing infrared photons, generating an electrical signal.[1] Narrowband detection, a desirable feature in these photodetectors, refers to their ability to selectively detect a narrow range of wavelengths, which enhances sensitivity and specificity in capturing desired spectral information. For example, HgCdTe is the commercially used compound material in the photodetectors of Fourier transform infrared spectrometers or night vision cameras. However, these HgCdTe-based photodetectors or cameras need to be cooled to near liquid nitrogen temperatures of ~77 K to reduce the thermally excited noise. In addition, these narrow-bandgap semiconductors usually contain hazardous elements such as As, Hg, Cd, and Te.

Unlike conventional materials, titanium oxides have emerged as promising narrow-bandgap alternatives due to their environmental safety. Titanium dioxide, TiO_2, is known to be nontoxic, widely available, cost-effective, and environmentally safe. This material has shown great promise in various areas, such as photovoltaics, visible-light photocatalysis, and biomaterials. Although significant research has been conducted on the wide-bandgap rutile form of TiO_2, its 3.3 eV bandgap is too large. Recently, great effort has been focused on improving the catalytic efficiency of TiO_2 by enhancing light absorption through doping or reduction.[10] For example, in reduced $TiO_{2\text{-}x}$, the isolated Ti^{3+} defect structure plays an important role in reducing the bandgap and increasing absorption in the visible range.[10] However, in this case, the Ti^{3+} ions are created within the Ti^{4+} structure of TiO_2, which significantly limits their effect. Recent research efforts aim to develop a stable and pure Ti^{3+} ($3d^1$) containing system such as titanium sesquioxide (Ti_2O_3).[11,12] Ti_2O_3 is a lesser-known titanium oxide with potential applications in photodetection and other electronic devices due to its unique optical and electronic properties.[11–13] Bulk Ti_2O_3 exhibits an insulator–metal transition at ~450 K, but unlike VO_2, it does not experience a structural phase transformation.[14–16] Upon heating, Ti_2O_3 transforms from an insulating state to a metallic state, showing typical semiconductor behavior with an ultranarrow bandgap at low temperatures.[11,15] This ultra-narrow bandgap and uniaxial anisotropy make Ti_2O_3 a promising candidate for specialized applications in infrared photodetectors and optical coatings.[16,17]

Metasurfaces can enhance scattering into the active layer of solar cells and photodetectors, improving their performance when used as a coating.[6,18–20] These surfaces are designed to support Mie resonances, which can control light at the subwavelength scale and increase the efficiency of light confinement and harvesting.[21–23] In periodic metasurfaces, the Rayleigh anomaly occurs when a diffraction order becomes grazing to the plane, strongly influencing light scattering and enhancing lattice resonances. By tuning the directionality of the scattering, resonant metasurfaces can more effectively channel light into active regions, boosting the overall efficiency of these devices.[24,25] The coupled multipolar models explain the collective optical response of periodic metasurfaces by describing the interaction between multipolar excitations of nanoantennas mediated by the lattice geometry.[21]

Here, we present the engineered structure of an infrared photodetector utilizing Ti_2O_3, with performance improvements achieved by integrating a resonant metasurface. Our findings indicate that the absorptance of the thin Ti_2O_3 layer increases significantly and almost reaches 100% due to the addition of the resonant metasurface, resulting in efficient scattering within the active layer. Furthermore, we demonstrate that the Ti_2O_3-based photodetector exhibits superior absorptance compared to photodetectors based on other commonly used infrared materials, such as InSb, InAs, and HgCdTe.

Epitaxial Ti_2O_3 thin films are grown on c-plane sapphire substrates by pulsed laser deposition (PLD) with a KrF excimer laser (Lambda Physik LPX 305, 248 nm, 30 ns FWHM). Details of the growth procedure can be found in Ref. 13. The chamber pressure is kept at high vacuum ($<10^{-8}$ Torr: 25 °C) during deposition, which is necessary to prevent the growth of impurity phases, such as anatase TiO_2 and rutile TiO_2. The laser beam is focused on a rotating Ti_2O_3 target (2.56 cm in diameter, Kurt Lesker) with a repetition rate of 5 Hz and laser fluence of 1.5 J/cm^2. The laser beam was rastered across the target surface in order to uniformly ablate the target surface while the target was rotated. For uniform film deposition, the substrate was also rotated during deposition at a speed of 20 rpm. The films are grown at a substrate temperature of 720 °C. After growth, the samples are kept at these temperatures for 30 min and then cooled at a rate of 10 °C down to room temperature in a ~10^{-8} Torr vacuum.

The crystal structure of the films is characterized by x-ray diffraction (XRD) measurements with Cu $K\alpha 1$ radiation (Bruker D8). Figure 1(a) shows a typical XRD pattern of a 200-nm-thick Ti_2O_3 thin film grown on an Al_2O_3 substrate at 720 °C. Peaks at ~41.68° and ~90.70° are indexed to the planes (0006) and (000,12) of the Al_2O_3 substrate, respectively. One can observe the film peaks at 37.9° and 81.0°, which correspond to the planes (011) and (022) of the orthorhombic phase (O-Ti_2O_3) ($Immm$ space group).[12] However, as shown in Fig. 1(b), when we zoom in 2θ angles around the (022) peak, a weak secondary peak is observed at ~79.8°, which is indexed as (111) TiO phase, indicating that the film grows mainly in orientation (011) of Ti_2O_3 with a secondary phase of TiO. The areal ratio of Ti_2O_3/TiO appears to be ~0.9. Similar mixed phases of T_2O_3 and TiO are consistent with the previous report on Ti_2O_3 films grown by PLD.[26]

The chemical structure of the grown films is characterized by Raman spectroscopy measurements (Witec, alpha 300) with a magnification of 100× and a laser wavelength of 532 nm. As shown in Fig. 1(c), four Raman peaks are observed at 247, 333, 446, and 612 cm^{-1}, which are assigned to orthorhombic Ti_2O_3.[12] These Raman spectra also confirm the orthorhombic Ti_2O_3 phase determined by XRD measurements. However, the TiO phase is not observed in Raman spectroscopy measurement due to the relatively small amount of TiO compared to Ti_2O_3. The surface morphology of the films is characterized using an Atomic Force Microscope (AFM, Bruker Dimension Icon) operated in peak force mode [Fig. 1(d)]. The film is composed of irregular shapes of large grains with a characteristic dimension of ~100 nm with rounded edges, and the film exhibits a relatively low surface roughness of ~2.3 nm.

The surface chemistry analysis of the films is performed using Al $K\alpha$ x-ray photoelectron spectroscopy (XPS) measurements. In order to remove contamination and eliminate surface oxidation effects, a high-energy argon (Ar) ion beam sputtering is applied for 210 s. Figure 1(e) shows the survey XPS spectra of the Ti_2O_3 film. As expected, before Ar-sputtering, a strong carbon peak is observed, and the ratio of O/Ti is close to Ti^{4+} (TiO_2 structure) due to surface oxidation. However, after Ar-sputtering, the carbon composition is reduced from 64 to 1 at. %, and the element ratio of O/Ti clearly decreases from 1.94 to 1.38 due to an increase in Ti^{3+} (Ti_2O_3 structure). As shown in Fig. 1(f), high-resolution XPS spectra of the Ti 2p region after Ar-sputtering verifies dominant Ti^{3+} states in Ti_2O_3 films.

The optical dielectric permittivity of the Ti_2O_3 films is determined by ellipsometry measurements by fitting the ellipsometry parameters Ψ and Δ into the Drude oscillator models. Spectroscopic ellipsometry is performed using a Variable-Angle Spectroscopic Ellipsometer (VASE, J.A. Woollam Co., Inc.) for wavelengths from 1.7 to 10 μm. The ellipsometry and reflectance data of the Ti_2O_3 films are analyzed using WVASE software. Figure 2(a) shows the real and imaginary parts of the dielectric permittivity for Ti_2O_3 thin films grown on the (0006) Al_2O_3 substrate.

A continuous 200-nm-thick film of Ti_2O_3 on top of the sapphire substrate absorbs approximately 25%–45% of incident light in the wavelength range of around 2–10 μm [Fig. 2(b)]. The further increase in absorptance is limited by the high reflection at the interface of Ti_2O_3 and free space, which have drastically different permittivities. Nanostructuring of the top layer can help reduce the reflectance and increase the amount of light propagating through the layer, but it is challenging to accomplish and not as effective as covering the layer with the metasurface, which efficiently scatters light into the active layer. The resonant metasurface made of material with negligible optical losses, such as silicon, can help channel more light into the active photodetector section and increase its efficiency, which we analyze below, showing that the absorptance of the thin Ti_2O_3 layer can reach almost 100%.

When designing the hybrid photodetector structure, it is crucial to evaluate and select appropriate theoretical models to predict and optimize the absorption spectra effectively. Various approaches can

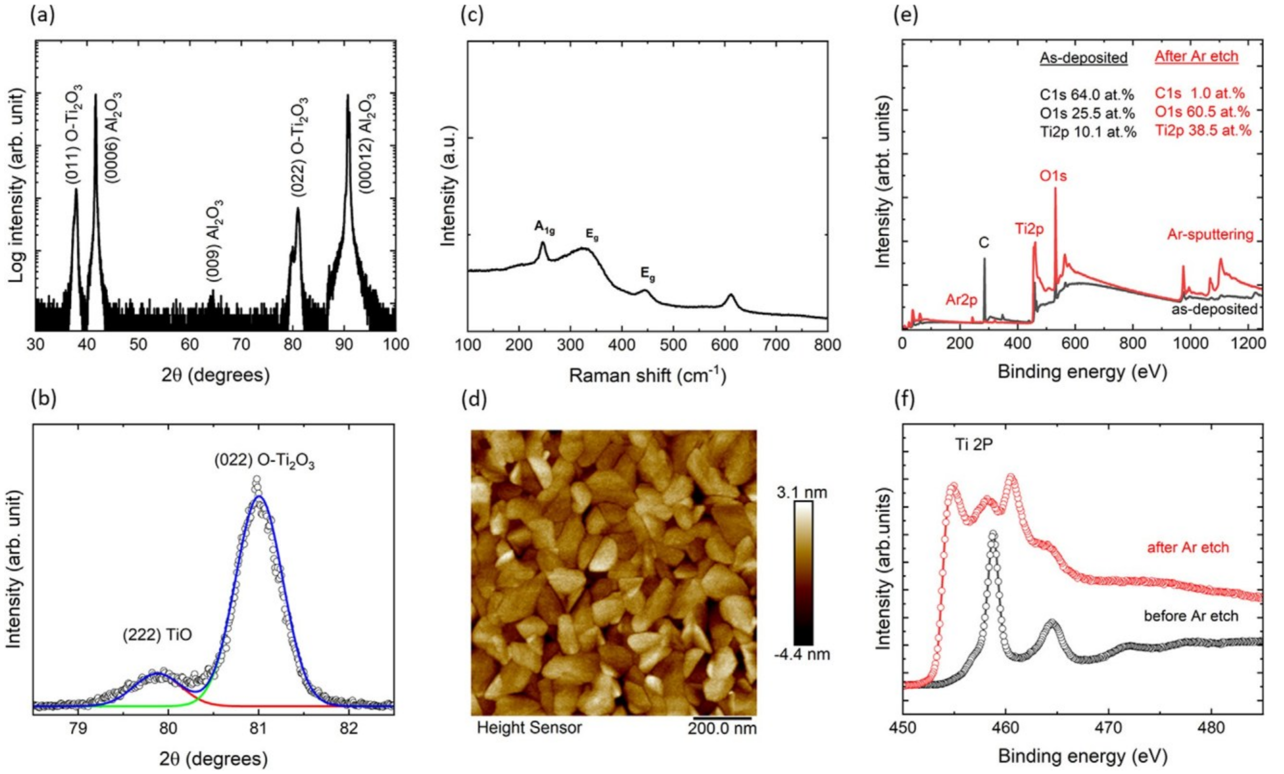

FIG. 1. XRD 2*h*-*x* scans of Ti$_2$O$_3$ film grown on (0006) Al$_2$O$_3$ substrate in (a) a wide 2*h* angle scan of 30°–100° and (b) a zoomed 2*h* angle scan of 79°–82°. (c) Raman spectra of the Ti$_2$O$_3$ films. (d) AFM image of the film surface showing uniform surface morphology with grain sizes of approximately ~100 nm. (e) Survey XPS spectrum of the Ti$_2$O$_3$ film before and after Ar ion etching. (f) High-resolution XPS spectra of the Ti 2p region before and after Ar etching. The etching time was 210 s.

guide this process, including impedance matching theory, resonant critical coupling theory, and others tailored to specific photodetector configurations, mainly describing how resonant modes interfere in the structure.[27–29] In regular periodic lattices composed of nanoantennas supporting Mie resonances, collective resonances emerge due to the coherent coupling between the localized Mie modes of individual nanoantennas and the diffracted orders of the lattice. These resonances are strongly influenced by the Rayleigh anomaly, which occurs when diffracted order transitions from evanescent to propagating at specific wavelengths, leading to enhanced in-plane scattering. The coupled

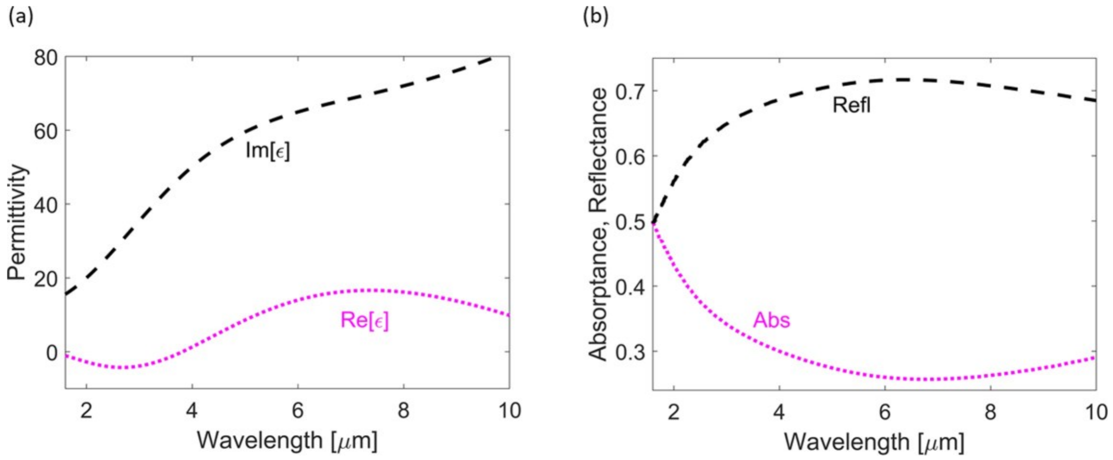

FIG. 2. (a) Permittivity *e* of the ~200-nm-thick Ti$_2$O$_3$ film grown on (0006) Al$_2$O$_3$ substrate by PLD. (b) Absorptance and reflectance of the same film on a sapphire substrate.

dipole–dipole model accurately describes these phenomena by considering the dipolar interactions between nanoantennas mediated through the lattice's periodicity in finite and infinite arrays.[21,30] This model captures the hybridization of localized Mie resonances with lattice modes, resulting in sharp spectral features and increased quality factors characteristic of lattice resonances. Considering these diverse models enables a comprehensive exploration of the interplay between material properties, geometric parameters, and optical responses, ultimately leading to more robust and efficient photodetector designs.

Let us consider the following design of the infrared photodetector consisting of an active layer of Ti_2O_3 and a silicon metasurface, enhancing light concentration in the active layer [Fig. 3(a)]. The thickness of the active layer (made of Ti_2O_3) is t, and it is grown on a sapphire substrate, which is considered infinite in modeling. The height of the silicon nanoantennas is a_z ¼ 400 nm, and it is fixed throughout the work. The nanoantennas have a square cross section with a_x and a_y, and they are arranged in a periodic array with d_x and d_y. Light is linearly polarized along the x-direction and is normally incident on the device surface. Rayleigh anomalies can be observed in the spectra of the nanoantenna array at wavelength when the first diffraction order emerges. The wavelength corresponding to the (1,0) Rayleigh anomaly, where (1,0) denotes the first diffraction order in the x-direction and no diffraction in the y-direction, is defined as k_{RA} ¼ nd, where n is the refractive index of the material where first diffraction order propagates, and d is the period of the array is the x- or y-direction (assumed equal throughout this work). Silicon nanoantennas are selected because of their high refractive index and low material losses in the infrared range.

To analyze the effect of the silicon metasurface, we first fix the period of the nanoantenna array at d_x ¼ d_y ¼ 3 lm and the thickness of the Ti_2O_3 layer at t ¼ 200 nm, and we vary the size of the silicon nanoantenna a_x ¼ a_y [Fig. 3(b)]. We observe that the absorptance enhancement occurs mainly near the Rayleigh anomalies. As the nanoantennas are in free space, the effect of the Rayleigh anomaly at

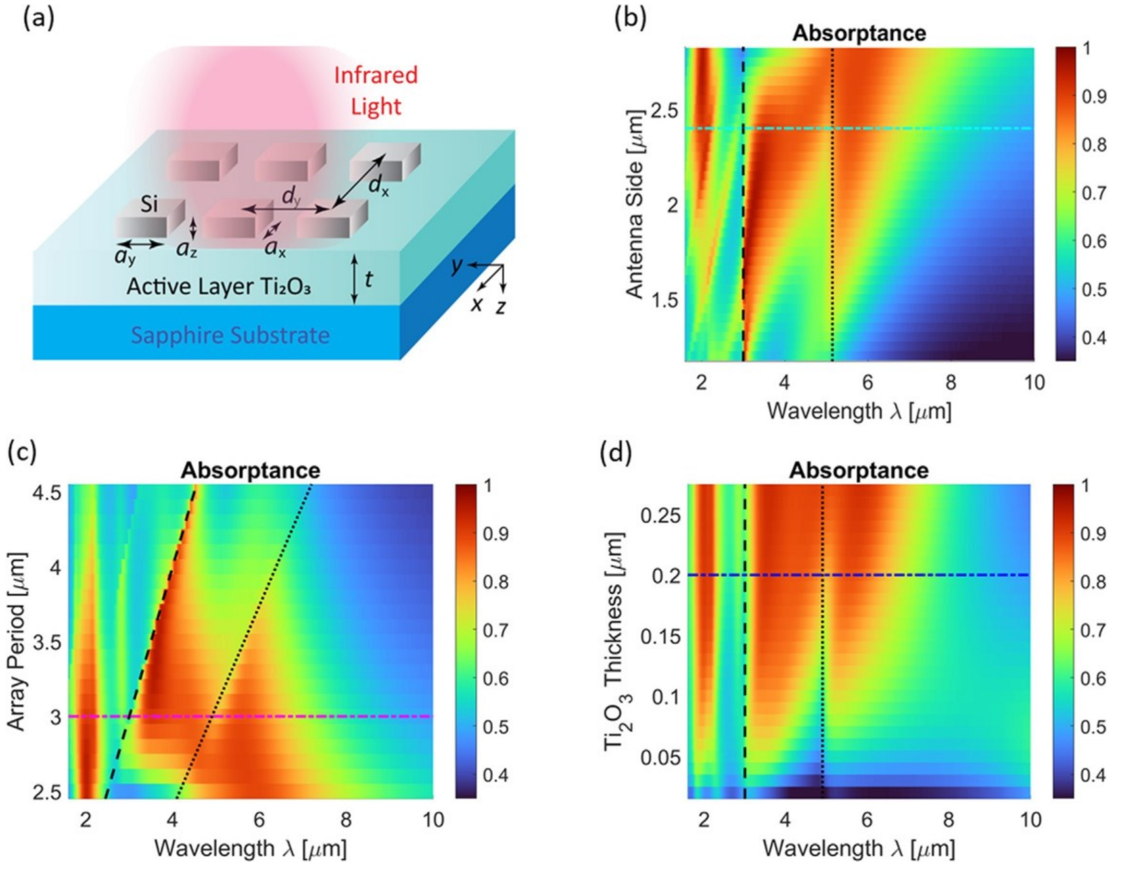

FIG. 3. (a) Schematic of the hybrid structure Si metasurface/Ti_2O_3/Al_2O_3 for enhanced absorptance in the infrared range. The top metasurface made of low-loss resonant nanoantennas (silicon) improves the scattering in the active Ti_2O_3 layer. (b) Absorptance of the nanoantenna array with a varying size of the silicon nanoantenna a_x ¼ a_y. The array period is fixed at d_x ¼ d_y ¼ 3 lm, and the vertical dashed and dotted lines correspond to Rayleigh anomalies (1,0) in the free space and the sapphire substrate, respectively. The horizontal dotted-dashed cyan line corresponds to a_x ¼ a_y ¼ 2.4 lm, providing optimal performance and is selected for the analysis of other parameters of the metasurface. (c) Absorptance of the nanoantenna array for a varying period. The diagonal dashed and dotted lines correspond to Rayleigh anomalies (1,0) in the free space and the sapphire substrate, respectively. The horizontal magenta dotted-dashed line corresponds to d_x ¼ d_y ¼ 3 lm, providing optimal performance, and is selected for analysis of other parameters of the metasurface. (d) Effect of varying the thickness of Ti_2O_3. Vertical dashed and dotted lines correspond to Rayleigh anomalies (1,0) in the free space and the sapphire substrate, respectively. The horizontal blue dotted-dashed line corresponds to t ¼ 200 nm, providing the optimal performance, and is selected for the analysis of other parameters of the metasurface.

k_{RA} ¼ 3 lm is stronger than the effect of the Rayleigh anomaly associated with the substrate. In the spectral region below the diffraction limit, the scattering in the active layer is not as effective as above the diffraction limit, and absorptance enhancement is observed only in narrow bands. For subsequent analysis, we select silicon nanoantennas with side lengths of a_x ¼ a_y ¼ 2.4 lm, which results in a higher absorptance of the active layer and, therefore, is expected to provide optimal photodetector performance.

The period of the nanoantenna array substantially affects the photodetector properties because the collective resonance of the nanoantennas can be spectrally tuned and shifted to a desired range. Our simulations show that a relatively dense array of nanoantennas is the most beneficial for increasing absorptance [Fig. 3(c)]. We observe the most efficient absorptance in the wavelength range of 3–6 lm. Efficient operation at the longer wavelength requires an increase in the array period and a simultaneous increase in the nanoantenna size. Furthermore, absorptance can be enhanced by utilizing a thicker Ti_2O_3 film, provided that its quality is not affected by the growth process and the accumulation of defects. The simulations show that the thickness of around 200 nm results in an almost complete absorptance of light. No further increase in thickness provides substantial enhancement [Fig. 3(d)]. Overall, the silicon metasurface with d_x ¼ d_y ¼ 3 lm and a_x ¼ a_y ¼ 2.4 lm and the thickness of Ti_2O_3 layer t ¼ 200 nm can provide the maximum absorptance of the proposed structure, and therefore, it can result in the optimal photodetector operation in the mid-wave infrared range.

The spectral response of the resonant metasurface without the inclusion of Ti_2O_3 is shown in Fig. 3(d) (see the case where the thickness of the material is zero). While the overall absorptance is significantly low, distinct spectral features remain observable. These features are particularly noteworthy, as the spectral positions of the resonances align closely with those observed in the hybrid structure containing Ti_2O_3. Thus, the hybrid structure retains the fundamental resonance characteristics of the metasurface without Ti_2O_3, with comparable widths and spectral positions, demonstrating that including Ti_2O_3 primarily enhances absorptance without fundamentally altering the underlying resonance behavior.

Finally, we compare several other materials that are known to be used in mid-infrared absorptance (Fig. 4). In the calculations, the InSb and InAs permittivity data are taken from Ref. 31, and the $Hg_{0.69}Cd_{0.31}Te$ permittivity data are taken from Ref. 32. We compare the cases with and without silicon metasurface (denoted "w/Si" and "w/o Si," respectively). The parameters of the silicon metasurface and the thickness of the active layer are the same for all materials, and they are set to d_x ¼ d_y ¼ 3 lm, a_x ¼ a_y ¼ 2.4 lm, and t ¼ 200 nm. We note that this comparison provides only absorptance of the active layer without accounting for the efficiency of carrier generation and other aspects of photodetection. Simulations show that the absorptance of Ti_2O_3 is much higher than that of other materials. This can be explained by the high material absorption and the metallic nature of Ti_2O_3. A continuous 200-nm-thick film of InSb on top of the sapphire substrate absorbs around 6% of the incident light at a wavelength of 2 lm, and this absorptance decreases as the edge of the bandgap approaches zero at a wavelength of ~7 lm. Similarly, InAs and HgCdTe absorb 8% and 12%, respectively, at 2-lm wavelength, and it drops at lower photon energies (reaching zero at ~3.5 and ~4 lm, respectively). By patterning the Si metasurface on top of these conventional semiconductor layers, the absorptance of these active layers is slightly increased up to 8%–18% in the range of 3–5 lm. In contrast, the Ti_2O_3 layer without the Si metasurface absorbs ~31% in the mid-wave infrared window (3–5 lm), and by fabricating the Si metasurface, the average absorptance in the MWIR window increases up to 86%. The average absorptance in the range of 3–5 lm for each material with optimized metasurface parameters is summarized in Table I. Overall, the absorptance of the Ti_2O_3 layer is several times higher than that of InSb, InAs, and HgCdTe with the same Si metasurfaces due to the narrow-bandgap characteristics of Ti_2O_3.

In conclusion, we have grown Ti_2O_3 thin films on a single crystal sapphire substrate by pulsed laser deposition. The 200-nm-thick Ti_2O_3 film on top of the sapphire substrate absorbs around 25%–45% of incident light in the wavelength range of around 2–10 lm. In order to

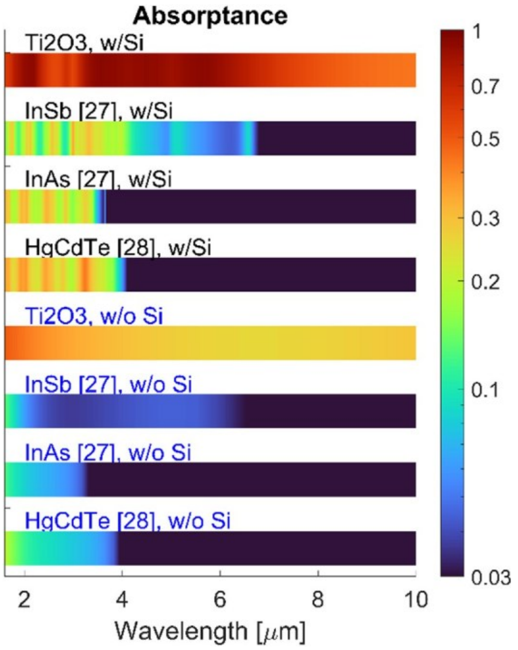

FIG. 4. Comparison of Ti_2O_3 with other materials commonly used in infrared photodetectors, such as InSb, InAs, and HgCdTe. The marks "w/Si" and "w/o Si" denote the case with and without the silicon metasurface, respectively. The parameters of the silicon metasurface and thickness of the active layer are the same for all cases.

TABLE I. Average broadband absorptance in the mid-wave infrared window (3–5 lm) for Ti_2O_3 and other conventional semiconductors, such as InSb, InAs, and HgCdTe, with and without Si metasurface. The silicon metasurface with d_x ¼ d_y ¼ 3 lm and a_x ¼ a_y ¼ 2.4 lm and the active layer of t ¼ 200 nm is considered in all cases. Labels "w/Si" and "w/o Si" denote the case with and without Si metasurface, respectively.

Active layer	Absorptance w/o Si	Absorptance w/Si
InSb	4%	18%
InAs	1.5%	8%
HgCdTe	4%	16%
Ti_2O_3	31%	86%

enhance light absorption in the Ti_2O_3 layer, we introduced a resonant metasurface on top of the Ti_2O_3 layer. Adding a resonant metasurface composed of a low-loss material significantly enhances absorptance by promoting efficient scattering within the Ti_2O_3 layer. Comparatively, the Ti_2O_3-based structure demonstrates superior absorptance in the infrared (2–10 μm) over conventional infrared semiconductors, such as InSb, InAs, and HgCdTe due to the narrow-bandgap characteristics of Ti_2O_3, which make Ti_2O_3 promising light absorbers in infrared photodetection applications.

This research was supported by the Office of the Undersecretary of Defense (Research & Engineering) ARAP program. V.E.B. acknowledges support through the ONR Summer Faculty Research Program and the National Science Foundation under Grant No. 2418519.

AUTHOR DECLARATIONS

Conflict of Interest

The authors have no conflicts to disclose.

Author Contributions

Viktoriia E. Babicheva: Conceptualization (equal); Formal analysis (equal); Investigation (equal); Writing – original draft (equal). Evgeniya Lock: Formal analysis (equal); Funding acquisition (equal); Writing – review & editing (equal). Heungsoo Kim: Conceptualization (equal); Investigation (equal); Writing – review & editing (equal).

DATA AVAILABILITY

The data that support the findings of this study are available from the corresponding author upon reasonable request.

REFERENCES

[1] C. Liu, J. Guo, L. Yu *et al.*, "Silicon/2D-material photodetectors: From near-infrared to mid-infrared," Light 10, 123 (2021).

[2] W. Xin, W. Zhong, Y. Shi *et al.*, "Low-dimensional-materials-based photodetectors for next-generation polarized detection and imaging," Adv. Mater. 36, 2306772 (2024).

[3] B. W. Jia, K. H. Tan, W. K. Loke *et al.*, "Monolithic integration of InSb photodetector on silicon for mid-infrared silicon photonics," ACS Photonics 5, 1512 (2018).

[4] B. W. Jia, K. H. Tan, W. K. Loke *et al.*, "Integration of an InSb photodetector on Si via heteroepitaxy for the mid-infrared wavelength region," Opt. Express 26, 7227 (2018).

[5] D. Palaferri, Y. Todorov, A. Bigioli *et al.*, "Room-temperature nine-μm-wavelength photodetectors and GHz-frequency heterodyne receivers," Nature 556, 85–88 (2018).

[6] S. Y. Wang, Q. Wang, H. Luo *et al.*, "InSb all-dielectric metasurface for ultrahigh efficient Si-based mid-infrared detection," Opt. Lett. 49, 2641–2644 (2024).

[7] A. Rogalski, "Infrared detectors: An overview," Infrared Phys. Technol. 43, 187–210 (2002).

[8] A. Haddadi, G. Chen, R. Chevallier *et al.*, "$InAs/InAs_{1-x}Sb_x$ type-II superlattices for high performance long wavelength infrared detection," Appl. Phys. Lett. 105, 121104 (2014).

[9] A. Rogalski, "HgCdTe infrared detector material: History, status and outlook," Rep. Prog. Phys. 68, 2267 (2005).

[10] N. Liu, C. Schneider, D. Freitag *et al.*, "Black TiO_2 nanotubes: Cocatalyst-free open-circuit hydrogen generation," Nano Lett. 14(6), 3309–3313 (2014).

[11] J. Wang, Y. Li, L. Deng *et al.*, "High-performance photothermal conversion of narrow-bandgap Ti_2O_3 nanoparticles," Adv. Mater. 29, 1603730 (2017).

[12] Y. Li, Y. Weng, X. Yin *et al.*, "Orthorhombic Ti_2O_3: A polymorph-dependent narrow-bandgap ferromagnetic oxide," Adv. Funct. Mater. 28, 1705657 (2018).

[13] D. J. Lahneman, H. Kim, H. Jiang *et al.*, "Electronic and optical properties of strain-locked metallic Ti_2O_3 films," Curr. Appl. Phys. 47, 9–14 (2023).

[14] J. M. Honig and T. B. Reed, "Electrical properties of Ti_2O_3 single crystals," Phys. Rev. 174, 1020–1026 (1968).

[15] M. Uchida, J. Fujioka, Y. Onose *et al.*, "Charge dynamics in thermally and doping induced insulator-metal transitions of $(Ti_{1-x}V_x)_2O_3$," Phys. Rev. Lett. 101, 066406 (2008).

[16] K. Yoshimatsu, H. Kurokawa, K. Horiba *et al.*, "Large anisotropy in conductivity of Ti_2O_3 films," APL Mater. 6(10), 101101 (2018).

[17] X. Yu, Y. Li, X. Hu *et al.*, "Narrow bandgap oxide nanoparticles coupled with graphene for high performance mid-infrared photodetection," Nat. Commun. 9, 4299 (2018).

[18] M. Ye, J. Zha, C. Tan *et al.*, "Graphene-based mid-infrared photodetectors using metamaterials and related concepts featured," Appl. Phys. Rev. 8, 031303 (2021).

[19] G. Zhang, C. Xu, D. Sun *et al.*, "Metasurface-tuned light-matter interactions for high-performance photodetectors," Fundam. Res. (published online 2024).

[20] R. Guan, H. Xu, Z. Lou *et al.*, "Design and development of metasurface materials for enhancing photodetector properties," Adv. Sci. 11, 2402530 (2024).

[21] A. Han, J. V. Moloney, and V. E. Babicheva, "Applicability of multipole decomposition to plasmonic-and dielectric-lattice resonances," J. Chem. Phys. 156(11), 114104 (2022).

[22] M. S. Islam and V. E. Babicheva, "Lattice Mie resonances and emissivity enhancement in mid-infrared iron pyrite metasurfaces," Opt. Express 31(24), 40380–40392 (2023).

[23] I. Allayarov, A. C. Lesina, and A. B. Evlyukhin, "Anapole mechanism of bound states in the continuum in symmetric dielectric metasurfaces," Phys. Rev. B 109(24), L241405 (2024).

[24] V. E. Babicheva and J. V. Moloney, "Lattice Zenneck modes on subwavelength antennas," Laser Photonics Rev. 13(2), 1800267 (2019).

[25] V. Karimi, "Optical chirality in MXene nanoantenna arrays," MRS Adv. 9, 557–564 (2024).

[26] J. Feng, L. Wang, Y. Song *et al.*, "Phase evolution with the film thickness in PLD-grown titanium oxides films," J. Alloys Compd. 831, 154727 (2020).

[27] S. Xiao, T. Liu, L. Cheng *et al.*, "Tunable anisotropic absorption in hyperbolic metamaterials based on black phosphorous/dielectric multilayer structures," J. Lightwave Technol. 37, 3290–3297 (2019).

[28] S. Xiao, T. Liu, X. Wang *et al.*, "Tailoring the absorption bandwidth of graphene at critical coupling," Phys. Rev. B 102, 085410 (2020).

[29] X. Wang, J. Duan, W. Chen *et al.*, "Controlling light absorption of graphene at critical coupling through magnetic dipole quasi-bound states in the continuum resonance," Phys. Rev. B 102, 155432 (2020).

[30] V. Karimi and V. E. Babicheva, "Dipole-lattice nanoparticle resonances in finite arrays," Opt. Express 31, 16857–16871 (2023).

[31] S. Adachi, "Optical dispersion relations for GaP, GaAs, GaSb, InP, InAs, InSb, $Al_xGa_{1-x}As$, and $In_{1-x}Ga_xAs_yP_{1-y}$," J. Appl. Phys. 66, 6030–6040 (1989).

[32] K. Moazzami, J. Phillips, D. Lee *et al.*, "Detailed study of above bandgap optical absorption in HgCdTe," J. Electron. Mater. 34, 773–778 (2005).